

# Time-Resolved Plasmonics used to On-Line Monitor Metal/Elastomer Deposition for Low-Voltage Dielectric Elastomer Transducers

Tino Töpfer, Samuel Lörcher, Hans Deyhle, Bekim Osmani, Vanessa Leung, Thomas Pfohl, and Bert Müller\*

Compliant hetero-nanostructures provide access to nano-photonics, flexible electronics, and artificial muscles. These nanometer-thin polymers and metals are regularly predicated on molecular beam deposition—a technique that leads reliably to homogeneous films and enables the precise in situ monitoring of forming nanostructures. Herein, it is demonstrated that spectroscopic ellipsometry can be used to on-line monitor film formation with a sub-nanometer resolution and the evolution of the related optical properties of the hetero-nanostructure. The data recorded include plasmonic fingerprints of Au islands as well as film formation on self-assembled polydimethylsiloxane (PDMS). Bi-functionalized thiol-PDMS, tailored for thermal deposition, serves as a self-assembled adhesion layer for Au electrodes. Suppressed localized plasmonic activity indicates the formation of a homogeneous Au film on thiol-PDMS and wrinkled Cr/PDMS, contrary to the well-known establishment of Au islands on bare PDMS. The tailored hetero-nanostructures based on Au/thiol-PDMS and Au on wrinkled Cr/PDMS adhesion layers enable the fabrication of stretchable electronics and low-voltage dielectric elastomer sensors and actuators for artificial muscles and tunable optics.

## 1. Introduction

Flexible and foldable conductors based on polymers are the foundation of “tissue-like” soft electronics.<sup>[1]</sup> Polydimethylsiloxane (PDMS) is used widely due to its low cost, ease of fabrication, biocompatibility, and optical transparency.<sup>[2]</sup> Areas of application have been extended from soft bioelectronics<sup>[3]</sup> and


microfluidics<sup>[4]</sup> to hybrid devices involving CMOS technology.<sup>[5]</sup> The high efficiency and reliability combined with 10% strain at millisecond response make silicone-based polymers promising for electrically activated elastomer (EAP)-based devices, such as tactile displays, adaptable lenses and sensors.<sup>[6]</sup> Manufactured in a low-voltage configuration, the remarkable ability of simultaneous sensing and actuating distinguishes EAPs and allows them to mimic natural muscle functionality.<sup>[7]</sup> Therefore, nanostructured, stacked actuators have been proposed as smart artificial muscle implants.<sup>[8]</sup> However, to guarantee the long-term stability of such low-voltage hetero-nanostructures, the sub-nanometer homogeneity of nanometer-thin polymer and metal films is required. Recently, the precisely tailored molecular weight distribution and functionality of thermally evaporated PDMS films has been demonstrated.<sup>[9]</sup> Contrary to micrometer-rough

PDMS thin films fabricated by electro-spray deposition,<sup>[10]</sup> the high degree of experimental control possible with organic molecular beam deposition (MBD) provides the opportunity to engineer self-assembled PDMS as well as metal films with nanometer precision.

Herein, we have fabricated thermally evaporated, self-assembled metal/PDMS nanostructures and monitored in situ the formation of deposited metallic layers from discontinuously arranged nanoparticles to confluent thin films by using spectroscopic ellipsometry (SE). Collective electronic oscillations induced by incident photons yield surface plasmon resonances (SPRs). Plasmonics is an application-rich merging of photonics and electronics<sup>[11]</sup> that allows one to track intrinsic structural properties such as the size and morphology of organic-inorganic hetero-nanostructures, without the restrictions imposed by the diffraction limit. Plasmonic oscillations can be tuned from the mid-infrared, which is of special interest for ultrafast data transfer in telecommunications based on semiconducting composites,<sup>[12]</sup> down to UV visibility<sup>[13]</sup> for bio-sensing applications<sup>[14]</sup> based on Au nanostructures. The combination of self-assembly by MBD, controlled by SE, paves the way for tailoring Au PDMS nanostructures towards homogeneous, multi-layer growth.

Dr. T. Töpfer, Dr. H. Deyhle, B. Osmani, Dr. V. Leung,  
Dr. T. Pfohl, Prof. B. Müller  
Biomaterials Science Center  
Department of Biomedical Engineering  
University of Basel  
Gewerbestrasse 14, 4123 Allschwil, Switzerland  
E-mail: bert.mueller@unibas.ch

S. Lörcher  
Chemistry Department  
University of Basel  
Klingelbergstrasse 80, 4056 Basel, Switzerland

 The ORCID identification number(s) for the author(s) of this article can be found under <https://doi.org/10.1002/aelm.201700073>.

DOI: 10.1002/aelm.201700073

Due to low PDMS surface energy,<sup>[15]</sup> adhesion promoters such as Cr are required to generate stable and compliant Au/PDMS composites. To circumvent the mechanical stiffness of Cr layers and the wrinkling of Cr/PDMS heterostructures, we synthesized bi-functional thiol-PDMS (SH-PDMS) with molecular weights tailored for MBD, to serve as soft self-assembled adhesion layers. Suppressed localized plasmonic activity in the visible spectral range indicates homogeneous Au growth on both the Cr and the thiol-PDMS adhesion layers, compared to Au cluster formation on bare PDMS. Remarkably, we determined a percolation threshold for the first confluent layer as low as a few nanometers of Au film thickness.

The methodology introduced herein optimizes the monitoring and tailoring of multi-layer plasmonic structures for soft nanophotonic and electronic applications. Dynamic control of the plasmonic behavior of Au nanostructures is of current scientific interest, due to their potential for optoelectronic devices such as photonic crystals, gratings and waveguides.<sup>[16]</sup> Au nanostructure shape control is also relevant for the development of biomimetic materials and printed electronics.<sup>[17]</sup> The combination of plasmonics with soft low-voltage EAPs offers the intriguing possibility of dynamically tuned plasmonic frequencies by manipulating the underlying polymer layer through structural and dimensional control.

## 2. Self-Assembly of Thermally Evaporated Thiol-PDMS

Besides optical properties, real-time SE detects the nanophotonic fingerprints of Au nanoparticles, which are related directly to the size, surface coverage and dielectric functions of nanoparticles. A schematic cross-section of the ultra-high vacuum (UHV) fabrication and in situ measurement configuration is shown in Figure 1a. We first investigate the self-assembly

of thermally evaporated SH-PDMS. Many approaches employed to control nanoscale architectures precisely are based on the high affinity of thiols to Au.<sup>[18,19]</sup> The synthesis of SH-PDMS from bi-functional hydroxy-ethoxy propyl-terminated polydimethylsiloxane (OH-PDMS) (Figure 2f) is characterized by nuclear magnetic resonance (NMR) and gel permeation chromatography (Figure 2 g,h). We emphasize in this study the demanded control of SH-PDMS molecular weight distribution (MWD) for thermal evaporation. Based on the thermal degradation temperature of 423 K (150 °C) for thiol groups,<sup>[20]</sup> the molecular weights required for linear SH-PDMS to evaporate are limited to about 3000 g mol<sup>-1</sup>.<sup>[9]</sup> The synthesized SH-PDMS (blue-colored curve in Figure 2h) reveals a number average molecular weight  $M_n$  of 2700 g mol<sup>-1</sup>, which offers a broad range of the MWD to be evaporated. After evaporation under UHV conditions at a temperature of 423 K (150 °C) (red-colored curve in Figure 2h), a slight shift to an  $M_n$  of 2800 g mol<sup>-1</sup> is found. In agreement with the NMR spectra, this shift results from a negligible amount of disulphide linkage-induced prolongation of SH-PDMS chains. However, as the molecular weight is shifted only slightly, and the reaction between disulphides or thiols with Au is similar,<sup>[21]</sup> the synthesized SH-PDMS is suitable for thermal evaporation.

The thermal evaporation and assembly of synthesized SH-PDMS on Au at an evaporation temperature of 393 K (120 °C) is illustrated in Figure 2a. A 1.2-nm-thin, surface-near layer with a refractive index  $n$  of 1.75 at a wavelength  $\lambda$  of 656 nm, combined with a superposed layer with  $n = 1.5$  at  $\lambda = 656$  nm, fits the experimentally obtained spectroscopic  $\Psi$ - and  $\Delta$ -values. The derived thickness of 1.2 nm corresponds to the (CH<sub>2</sub>)<sub>3</sub>-O-(CH<sub>2</sub>)<sub>2</sub>-SH (2-propoxyethyl-1-thiol) terminal group with a theoretical length of 1.04 nm. The refractive index of the overlying layer relates to the dimethylsiloxane repeating units of SH-PDMS superimposed with the optical properties of free (CH<sub>2</sub>)<sub>3</sub>-O-(CH<sub>2</sub>)<sub>2</sub>-SH groups. Re-evaporation of the adsorbed,

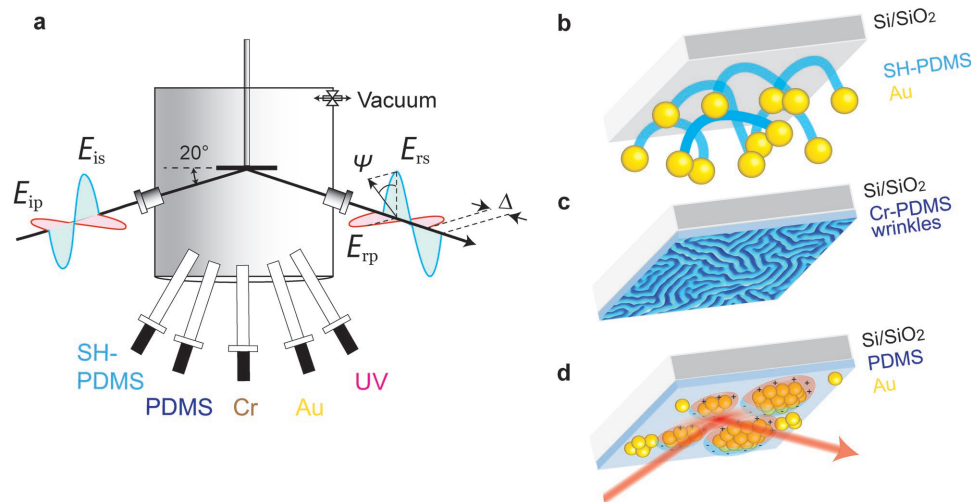


**Figure 1.** Thin film preparation scheme. a) Cross section of the organic molecular beam deposition setup for the fabrication of soft multi-layer nanostructures under ultra-high vacuum conditions. In situ spectroscopic ellipsometry at an incident angle of 20° simultaneously monitors film thickness, optical properties, and plasmonics. Representative schemes of thermally grown soft nanostructures: b) self-assembled Au particles bound to bi-functional, thiol-terminated PDMS; c) wrinkled Cr/PDMS; d) Au nanoparticles on a PDMS membrane. Coherent electron oscillations occur if the nanoparticles become excited at the resonance frequency. Due to the incident 4 × 10 mm<sup>2</sup> beam dimension, SE monitors nanostructures over a macroscopic area.

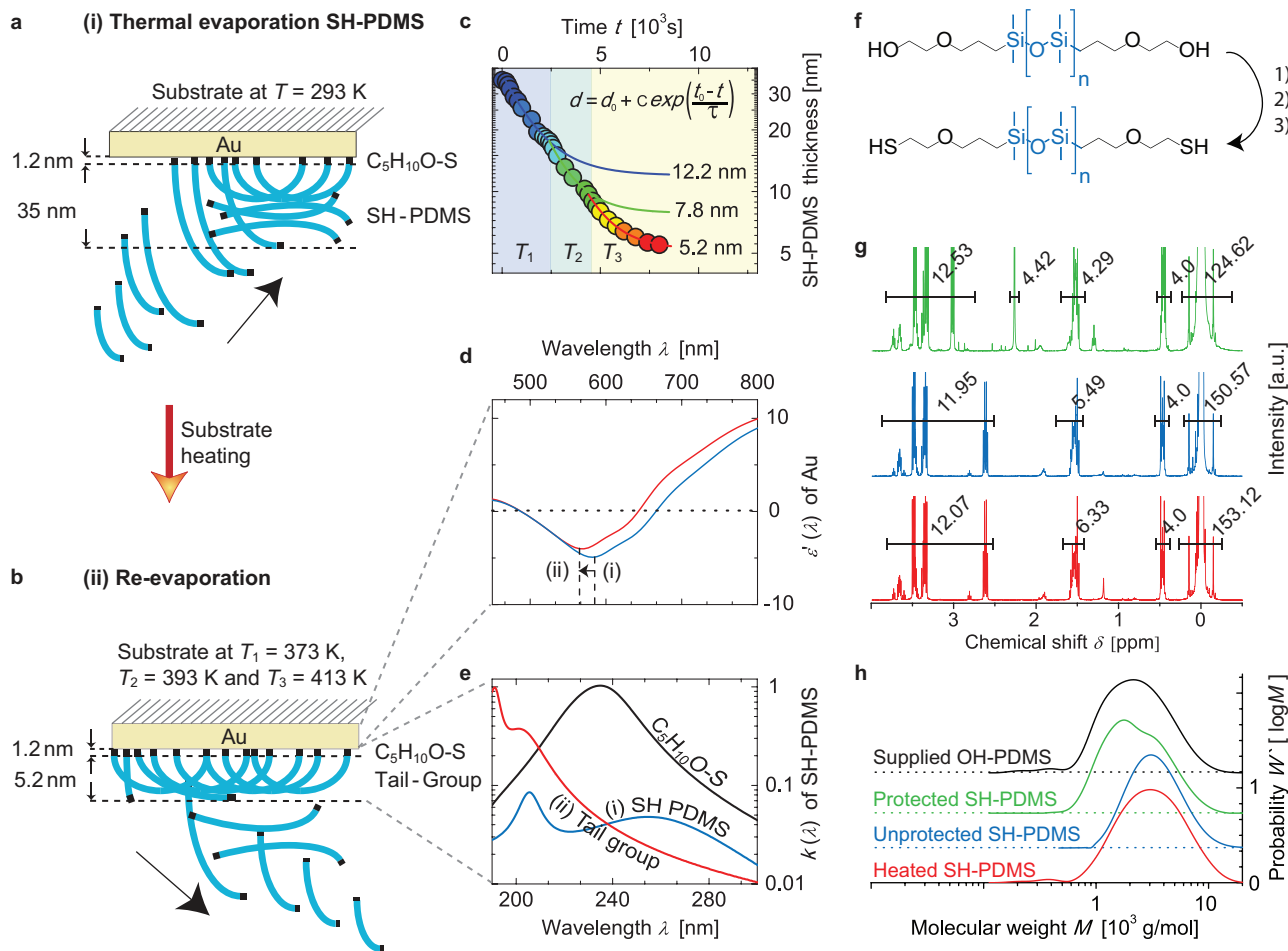


**Figure 2.** Self-assembly of bi-functional thiol-terminated PDMS on Au. a) Stacking schemes of i) thermally evaporated SH-PDMS chains consisting of the  $(\text{CH}_2)_3\text{O}-(\text{CH}_2)_2\text{-SH}$ -group (black) and dimethylsiloxane repeating units (blue) on an Au substrate. b) Monolayer of SH-PDMS chains double-bounded to Au after ii) the re-evaporation of excess molecules. c) Time-resolved desorption of SH-PDMS chains at substrate temperatures 373 K (blue), 393 K (green) and 413 K (red). d) SPRs in the dielectric function of the underlying Au reveal environmental dielectric properties,<sup>[46]</sup> for example a SPR-red shift due to the increasing environmental refractive index of S–Au bonds.<sup>[47]</sup> However, the distinct SPR blue shift from 590 to 580 nm during the re-evaporation process rather relates to Au-clustering as a result of substrate heating.<sup>[26]</sup> Thus, considering all structural transitions is crucial to conclude the formation process of Au/SH-PDMS nanostructures. e) Extinction coefficient of the bi-layer model for SH-PDMS (blue), consisting of the  $(\text{CH}_2)_3\text{O}-(\text{CH}_2)_2\text{-SH}$  group (black) and the tail group (red). The dielectric function is determined based on Tauc–Lorentz oscillators.<sup>[44]</sup> f) Synthetic route to yield the bi-functional, thiol-terminated PDMS (SH-PDMS) from bi-hydroxy-ethoxy propyl-terminated PDMS (OH-PDMS) with 1) trifluoromethanesulfonic anhydride at  $-20\text{ }^\circ\text{C}$  for 3 hours; 2) potassium thioacetate at  $25\text{ }^\circ\text{C}$  for 12 hours; 3)  $\text{LiAlH}_4$  at  $0\text{ }^\circ\text{C}$  for 4 hours. g) Nuclear magnetic resonance spectra of protected bi-functional thiol-terminated polydimethylsiloxane (green), unprotected bi-functional thiol-terminated polydimethylsiloxane (blue) and bi-functional thiol-terminated polydimethylsiloxane (red), thermally treated at a temperature of 423 K ( $150\text{ }^\circ\text{C}$ ) for a period of 40 minutes. h) The corresponding molecular weight distributions obtained from gel permeation chromatography traces. The black curve represents bi-functional hydroxy-ethoxy propyl-terminated polydimethylsiloxane (OH-PDMS) as supplied.

free SH-PDMS chains yields a self-assembled layer of Au-S-PDMS. The stepwise reduction in film thickness for increased substrate temperatures related to SH-PDMS desorption is presented in Figure 2c. Van-der-Waals interactions of the methyl side groups dominate intermolecular interactions between SH-PDMS on the substrate and in the crucible melt.<sup>[9]</sup> Therefore, an entire desorption of free SH-PDMS is assumed for substrate temperatures well above the evaporation temperature of 393 K. The S–Au bond strength of  $167\text{ kJ mol}^{-1}$ <sup>[18]</sup> enables substrate heating above 413 K ( $140\text{ }^\circ\text{C}$ ) before the S–Au bond fractures. The SH-PDMS film thickness diminishes asymptotically to 5.2 nm, whereas the thickness of the surface near the  $(\text{CH}_2)_3\text{O}-(\text{CH}_2)_2\text{-S}$  layer remains constant. This behavior

indicates a self-assembled layer with ordered SH-PDMS linked to Au. According to literature, the peak molecular weight of linear PDMS evaporated at 393 K is  $1600\text{ g mol}^{-1}$ ,<sup>[9]</sup> corresponding to a chain length of about 9.5 nm.<sup>[22]</sup> Assuming a characteristic  $30^\circ$  tilting angle, as for self-assembled alkene thiols,<sup>[18]</sup> a layer thickness of 8.2 nm is calculated, which is thicker than the experimentally determined example. During re-evaporation the distinct UV absorption of the  $(\text{CH}_2)_3\text{O}-(\text{CH}_2)_2\text{-SH}$  group around a wavelength of  $240\text{ nm}$ <sup>[23]</sup> decreases within the tail-group layer (Figure 2e). In combination with the final layer thickness of 5.2 nm, this behavior implies bent, double-bonded residual SH-PDMS chains on Au after re-evaporation. The evaporation of 13.3-nm-long SH-PDMS chains at

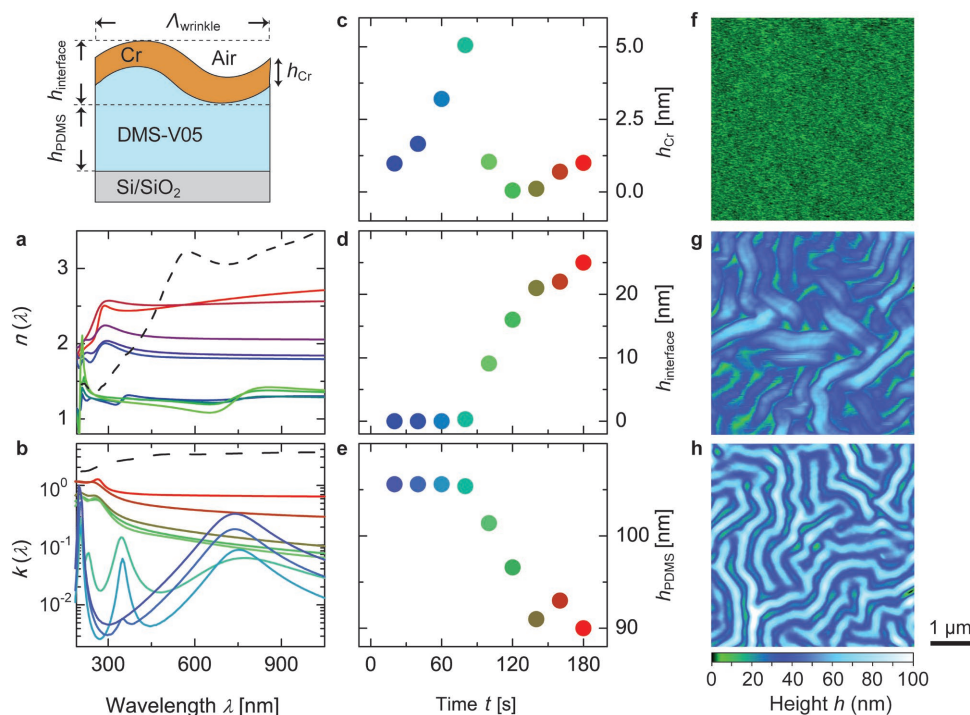


**Figure 3.** Morphology evolution of isotropic Cr/PDMS-nanostructures. a) Spectroscopic data of refractive index  $n$  and b) extinction coefficient  $k$  data of thermally deposited Cr on UV-cured PDMS (DMS-V05) are shown for deposition periods between 20 and 180 s (blue to red-coloured in (c–e) with 20 s intervals. The dashed line corresponds to Cr bulk values.<sup>[48]</sup> The ellipsometry model (inset) consists of three layers: c) Cr film with thickness  $h_{Cr}$ , d) a Cr/PDMS compound layer with thickness  $h_{interface}$ , gradually changing the optical properties from Cr to that of e) PDMS film with thickness  $h_{PDMS}$ . Atomic force microscopy images reveal the morphological transformation from f) a flat PDMS film with a surface roughness of 0.7 nm to g) a wrinkled 12 nm-thin Cr-PDMS surface in the terminal stage. Fourier transform analysis of a series of images reveals a wrinkle period of  $(470 \pm 20)$  nm. This micro-structured Cr surface, with dimensions in the range of the incident light wavelength, induces distinct absorbance due to light scattering. In addition, these wrinkles can fulfil the surface plasmon excitation condition as published for Ag pattern on elastomers.<sup>[49]</sup> (h) Morphology in equilibrium was measured two weeks after preparation. The wrinkle period remains  $(470 \pm 20)$  nm, but the shape evolves from a sinusoidal to a top-hat profile, with average amplitudes increasing from 50 to 80 nm.

an evaporation temperature consistent with the substrate temperature of 413 K leads to a layer thickness of 7 nm. Hence, SH-PDMS assembly on gold can be tailored precisely via the interplay between evaporation and substrate temperature. Stacked mirrored, as displayed schematically in Figure 1b, the SH-PDMS layer is anticipated to provide localized Au nanoparticle bonding, resulting in a homogeneous SH-PDMS/Au architecture.

### 3. Chromium Film Morphology Evolution on PDMS

Alternatively, a matured approach to promote adhesion between thin Au films and soft PDMS membranes involves the incorporation of nanometer-thin Cr-films. The additional metal interlayer, however, induces significant stiffening. Fabricated as a pre-stretched wrinkled microstructure, Cr-PDMS can retrieve some flexibility under strain.<sup>[24]</sup> PDMS pre-stretching, to build oriented wrinkles, is difficult to manage with nanometer-thin PDMS membranes. The spontaneous, isotropic formation of wrinkles can be induced through heating during metal deposition,<sup>[25]</sup> due to the evaporator's infrared (IR) radiation. A time sequence during Cr deposition, with a constant rate of

$0.062 \text{ nm s}^{-1}$ , is shown in Figure 3. The tri-layer model applied to the ellipsometry data allows for distinguishing between a flat Cr film with height  $h_{Cr}$  and a wrinkled Cr-PDMS interface layer with height  $h_{interface}$ . This straightforward model is justified, as the PDMS surface roughness of  $(0.7 \pm 0.1)$  nm, determined by AFM (Figure 3f), remains well below the dimensions of the wrinkled surface morphology. The graphs in Figure 3c–e elucidate the onset of wrinkle formation at 80 s after deposition commencement. The decreased PDMS film thickness  $h_{PDMS}$  and Cr film height  $h_{Cr}$  can be characterized as the formation of a wrinkled interface layer. We assume that a confluent Cr film forms for deposition of 80 s, which is associated with increasing IR-light shielding. Subsequently, the PDMS film relaxes evolving isotropic wrinkles, a scenario supported by the on-line measurement of the refractive index  $n(\lambda)$  and extinction coefficient  $k(\lambda)$  that reveal SPR at  $\lambda = 740$  nm after 20 s deposition continuously shifting to  $\lambda = 800$  nm after an 80 s deposition time (Figure 3a,b). This observed redshift implies the formation of Cr nanoparticles. Delocalized electrons of the near infrared (NIR) Drude-band in the extinction spectra occur at deposition times above 80 s, which is an indication of the coalescence of Cr nanoparticles for films thicker than 5 nm. An additional resonance peak at  $\lambda = 260$  nm arises for depositions exceeding 80 s. The corresponding refractive index at this wavelength is



larger than that of bulk Cr for the thicker films, a finding we link to wrinkled Cr-morphology rather than to Cr's dielectric function, a notion supported by the AFM image in Figure 3g. Isotropic wrinkles dominate the final Cr-PDMS topography.

#### 4. Au Formation on Soft Hetero-Nanostructures

The multi-layer hetero-nanostructures investigated herein are depicted schematically in Figure 4. Au depositions on SiO<sub>2</sub> and on a UV-cured PDMS 98-nm-thin membrane are shown in Figures 4a,b. The related ellipsometry measurements serve as references for Au deposited on rigid and soft substrates.<sup>[26,27]</sup> The Au film formation schemes for three differently built soft nanostructures are illustrated in Figures 4c–e. Ellipsometry gives rise to the dielectric constant  $\epsilon'$  and the extinction coefficient  $k$  spectra of Au films up to a thickness of 22 nm. Ellipsometry-derived values for film thickness are based on the Drude–Lorentz oscillators model and validated by AFM

measurements at the edges. Furthermore, AFM images, as represented in the fourth row of Figure 4, confirm the ellipsometer-derived data on surface roughness. The employed Lorentz oscillators adapt excellently to the plasmonic absorption bands, resulting in mean square errors well below unity for the modeled hetero-nanostructures (Supporting Information, Figure S1). UV-interband transitions from  $d$ -valance to  $s$ - and  $p$ -bands above the Fermi level of Au occur at resonance energies of 3.05 and 4.30 eV (406 and 288 nm), modeled by two Lorentz dispersions.<sup>[28]</sup> Further discussions focus on the intrinsic properties of Au nanoparticles with plasma frequencies in the range of visible light. SE provides a sensitive but non-invasive characterisation technique without influencing the intrinsic properties of the nanostructures, because local heating, owing to plasmon resonance absorption, can be neglected.

For the deposition of Au on SiO<sub>2</sub>, a single SPR, consisting of two Lorentz oscillators (Supporting Information, Figure S3e), exhibits redshift and broadens in line with increasing average film thickness (Figure 4a). For films thicker than 16 nm, the

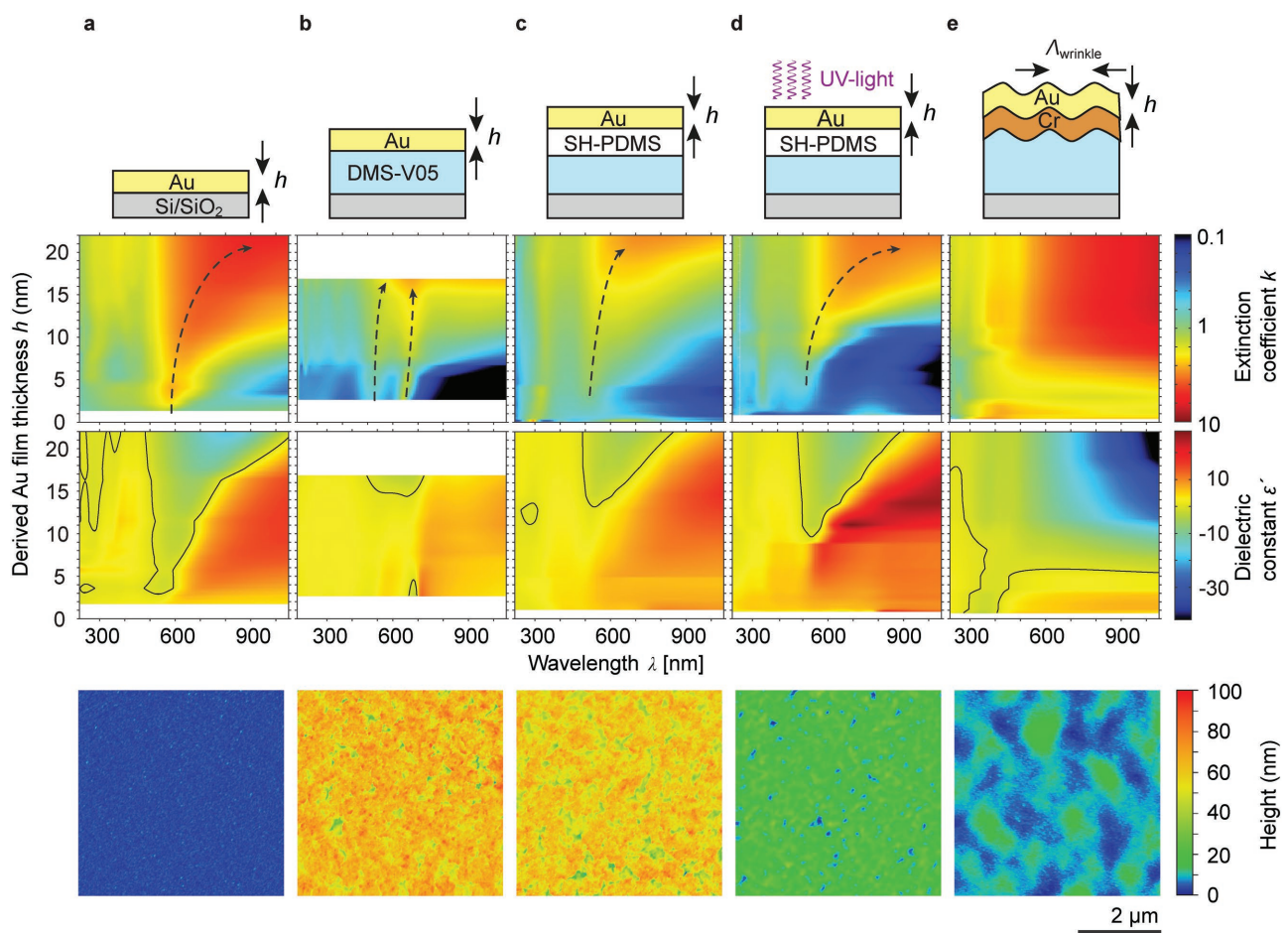


**Figure 4.** Plasmonics of growing Au nanoparticles on soft hetero-nanostructures. Film-thickness-dependent spectroscopy of the extinction coefficient  $k$  (second row) and the real part  $\epsilon'$  of the dielectric function (third row) are shown for thermally evaporated Au nanoparticles on a) Si/SiO<sub>2</sub>; b) UV-cured thermally evaporated DMS-V05; c) thermally evaporated SH-PDMS; d) SH-PDMS deposition during UV-radiation (termed as UVSH-PDMS); e) isotropic wrinkled Cr-PDMS nanostructures. The colour code for the extinction coefficient  $k$  is displayed logarithmically and the real part  $\epsilon'$  of the dielectric function linearly. Dashed arrows indicate the occurrence and shift of SPR peak frequencies within the extinction coefficient spectra. The boundary for which the dielectric constant appears,  $\epsilon' < 0$ , is marked as a black line. This event is connected to delocalized electron oscillations that occur in the NIR Drude-band. The final Au film morphologies on the corresponding hetero-nanostructures are characterized by atomic force microscopy (fourth row).

second oscillator evolves into the NIR Drude-band. The redshift of the SPR in the extinction spectrum goes along with changes in  $\epsilon'$  from positive to negative, explained by the coalescence of metal nanoparticles and relating to localized free electrons. The percolation threshold can be defined as an insulator-to-metal transition (IMT) and implies delocalized free electrons for  $\epsilon' < 0$  in the NIR.<sup>[29]</sup> For Au/SiO<sub>2</sub> the IMT is observed for films thicker than  $(20.0 \pm 0.5)$  nm. Höver et al. have already found an IMT for Au/SiO<sub>2</sub> for 8 nm-thin Au films.<sup>[30]</sup> However, their analysis is based on  $\epsilon'$ -shifts at a light wavelength of 20  $\mu\text{m}$ , for which transition behavior is increasingly pronounced and occurs for thinner Au layers.

The properties of Au on an UV-cured PDMS membrane are illustrated in Figure 4b. Two main SPRs at wavelengths of 540 and 650 nm for 2.7 nm-thin films are observed. Using selected deposition times (Supporting Information, Figure S2), the evolution of the SPRs can be followed in detail. Increasing film thickness, these SPRs redshift and merge to a single peak. Simultaneously, a third SPR band in the NIR develops above an Au thickness of 10 nm. Although the blue shift of SPRs with increasing particle heights counters the redshift of lateral growth, it has been stated that lateral particle size dominates the shift of SPRs,<sup>[26]</sup> e.g. SPR absorption splits into two bands for elongated nanometer-sized clusters.<sup>[31]</sup> Detected SPRs at an Au thickness of 2.7 nm suggest clusters with a lateral aspect ratio of 1.9. The third resonance may be due to cluster coalescence with increasing aspect ratios from 1.9 to 4.0 for 16.7 nm-thin Au.<sup>[31]</sup> The analysis of related AFM images (Supporting Information, Figure S2e,f) reveals an aspect ratio of  $(2.1 \pm 0.5)$  - a significantly smaller value for terminal film thickness. Thus, a contribution of Au multipoles coalescing to distances below a few nanometer should be considered, which likewise splits

and redshifts SPRs.<sup>[32]</sup> Hence, in order to extract the shape, size and distance of Au islands in situ from multiple SPRs in the SE data, the predominant growth mode needs to be classified by a real-space imaging technique.

Compared to islanding on pure PDMS membranes, SH-PDMS promotes Au adhesion. One SPR is detected splitting up into two Lorentz oscillators for films above 4 nm (Figure 4c). The IMT for Au/SH-PDMS was extrapolated to a film thickness of  $(25 \pm 1)$  nm. However, the onset for localized electron oscillations at an SPR wavelength of 633 nm is derived already for Au films  $(15 \pm 1)$  nm thin.

## 5. From Individual Gold Clusters to a Confluent Layer

To shed light on the process of Au islanding, the experimental data derived from ellipsometry are analysed. **Figure 5** contains the data of Au film formation on five selected substrates. Although the Au evaporator provides a constant deposition rate, the measurement reveals a three to four times larger growth rate during early stages than for advanced multilayer growth. This phenomenon can be attributed to the relatively low surface energy of bare PDMS, which promotes Au islanding, known as Volmer–Weber growth.<sup>[33]</sup> With increasing Au cluster density the probability of coalescence increases. At certain coverage, the percolation threshold is reached and further deposition will result in a layer of connected Au clusters, schematically represented in Figure 5a. We determine the percolation threshold from the intersection of the ellipsometry-derived deposition rate  $h'$  with the expected mean deposition rate  $d'$ . For Au/SH-PDMS the percolation threshold

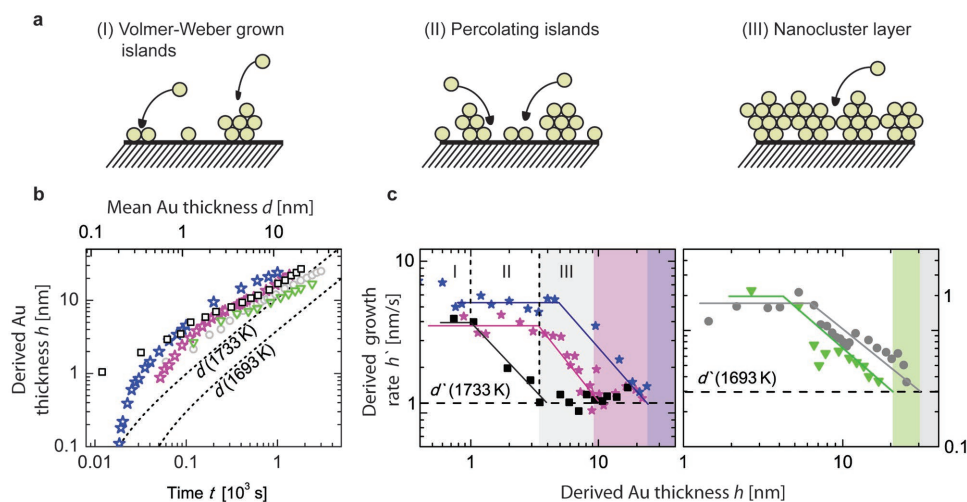


**Figure 5.** Au nanocluster percolation threshold. a) Schematics of Au film formation from 3D islanding (Volmer–Weber mode) towards the assembly of a nanocluster layer are illustrated. b) Ellipsometry-derived Au film thickness  $h$  at representative time points for Au growth on Si/SiO<sub>2</sub> (grey circles), UV-cured thermally evaporated PDMS (green triangles), 7-nm-thin thermally evaporated SH-PDMS (blue stars), 7-nm-thin thermally evaporated SH-PDMS with synchronous UV-irradiation, termed UVSH-PDMS (violet stars), where an isotropic wrinkled Cr-PDMS nanostructure (black squares) is shown. Dotted lines illustrate expected mean Au thickness  $d$  as adjusted by the evaporator temperature corresponding to the top axis of the diagram. c) Ellipsometry-derived growth rates  $h'$  of Au on hetero-nanostructures are shown. Expected mean growth rates  $d'$  for evaporation temperatures of 1733 and 1693 K are marked as dashed lines. The proposed three growth phases are representatively marked for Au growth on Cr-PDMS wrinkles: I) the 3D-pronounced formation of freestanding gold islands introduces higher growth rates than adjusted; II) the percolation of Au nanoclusters directs growth towards III) a 2D-pronounced assembly to a confluent cluster layer. The percolation threshold to confluent 2D-pronounced assembly is claimed as the match between the derived growth rate  $h'$  and the expected mean growth rate  $d'$  (colour-shaded areas).

corresponds to  $(24 \pm 1)$  nm, in agreement with the observed IMT value. The comparable value of  $(22 \pm 1)$  nm for Au/PDMS is an indication of an almost identical process of Au nanocluster formation. The distinct extinction feature, i.e. the band around a wavelength of 280 nm for all Au thicknesses investigated, is associated with the  $(\text{CH}_2)_3\text{-O-(CH}_2)_2\text{-S}$ -group of SH-PDMS (Figure 4c). This absorption feature indicates an entangled layer of Au and SH-PDMS. The comparably low van-der-Waals interactions between free SH-PDMS chains enable their flexible arrangement according to cohesive forces of attached Au adatoms towards Au nanocluster assembly similar to the growth on pure PDMS. The related AFM images exhibit a roughness of  $(8.1 \pm 1.0)$  nm, consistent with  $(7.9 \pm 0.8)$  nm for Au/PDMS. Because the cohesive forces between Au atoms are smaller than the strong S-Au bonds,<sup>[34]</sup> Au nanoclusters are well connected to SH-PDMS chains, and they can form a conducting matrix of nanometer-sized clusters.

To build well-ordered, confluent Au monolayer on SH-PDMS, UV radiation has been applied to the hetero-nanostructure subsequent to the deposition of the Au cluster monolayer (Figure 4d). SH-PDMS can be cross-linked via methyl side groups to the underlying PDMS membrane, termed UVSH-PDMS. A rearrangement of UVSH-PDMS chains is presumably suppressed and may lead to localized Au through strong S–Au bonds. In fact, the decrease in oscillations from localized electrons at a wavelength of 633 nm implies a reinforced homogeneous growth mode. Especially for films thinner than 8 nm, the plasmonic activity of localized electrons is reduced by one order of magnitude compared to Au/PDMS. In addition, the absorbance band at wavelengths between 280 and 300 nm is less pronounced for Au/UVSH-PDMS. This observation indicates a sharp interface between Au and UVSH-PDMS. Although the IMT at a film thickness of  $(25 \pm 1)$  nm is consistent with Au/SH-PDMS and Au/PDMS, the determined percolation threshold is only  $(12 \pm 1)$  nm (Figure 5c). The surface roughness obtained from AFM experiments corresponds to  $(4.4 \pm 0.3)$  nm for Au/UVSH-PDMS, roughly a factor of two smaller than for Au/SH-PDMS and Au/PDMS.

For Au deposition on wrinkled Cr/PDMS heterostructures, an IMT can be observed for films thicker than  $(5.2 \pm 0.3)$  nm (Figure 4e). The percolation threshold of  $(4.4 \pm 0.3)$  nm (Figure 5c) is even below this value and a factor of five smaller compared to Au/PDMS. SPRs in the visible range of the extinction spectrum are entirely suppressed; however, above the percolation threshold, absorbance is significantly increased with respect to Au on SH-PDMS. This effect can be related to the propagation of surface plasmon oscillations within the underlying Cr film. Another resonance in the UV-range occurs at Au film thicknesses as low as 0.7 nm. Centred on a wavelength of 320 nm, the absorbance peak exhibits redshift as the deposition proceeds. This resonance can originate from the wrinkled Cr microstructures with increasing wrinkle wavelengths during Au deposition, as evidenced by AFM images. The isotropic wrinkles (Figure 3g) disappear and an Au film with a roughness of only  $(2.9 \pm 0.2)$  nm remains (Figure 4e). The relaxation of wrinkles can be understood as pre-stretching of the underlying elastic Cr/PDMS membrane, due to the heat load during Au deposition.<sup>[35]</sup>

## 6. Conclusion

Organic and metal molecular beam deposition, controlled via real-time spectroscopic ellipsometry, paves the way for tailoring multi-layered metal/elastomer heterostructures with nanometers in thickness and to quantify the formation process of these heterostructures. The present growth and built-up study demonstrates that the in situ ellipsometry analysis of optical properties and plasmonic fingerprints can reach sub-nanometer resolution, which in this case was additionally complemented by the real-space AFM technique. Functionalized organic building blocks can substantially improve the homogeneity and stability of Au films deposited on an elastomer such as PDMS. We anticipate maintained compliance either by localized Au-S bonds or pre-stretched, nanometer-thin Cr, which is especially beneficial for future soft electronics. These specifically tailored soft nanoscale heterostructures in low-voltage DEA configurations are anticipated for potential nanophotonic devices, including soft tunable gratings for nano-optics<sup>[36]</sup> and tunable plasmonic absorbers.<sup>[37]</sup> Moreover, sensing and actuating can be achieved within a single DEA heterostructure, and the fabrication of biomimetic compliant transducers similar to human tissue is key to realizing artificial muscles<sup>[38]</sup> and soft robotics.<sup>[39]</sup>

## 7. Experimental Section

**Supplied materials:** Supplied vinyl-terminated PDMS DMS-V05 (Gelest Inc., Morrisville, PA, USA) was utilized without additional purification steps. Au and Cr were supplied by Kurt J. Lesker Company, UK. As substrates, 2-inch n-doped Si-wafers (SIEGERT WAFER GmbH, Aachen, Germany) with a thickness of  $(279 \pm 25)$   $\mu\text{m}$  were used.

**Synthesis of thiol-terminated polydimethylsiloxane:** Bi-functional, hydroxy-ethoxy propyl-terminated polydimethylsiloxane (PDMS) cArbinol Fluid 5562, referred to as "OH-PDMS," was supplied by Dow Corning, Germany. The other chemicals and dry solvents were bought from Sigma-Aldrich in the highest grade available and used as supplied. The solvents were distilled from technical-grade supplies. The PDMS structure was confirmed by <sup>1</sup>H nuclear magnetic resonance (<sup>1</sup>H NMR): (400 MHz,  $\text{CDCl}_3 + \text{K}_2\text{CO}_3$ ,  $\delta$ , ppm):  $-0.50$ – $0.35$  (m, 122.70 H,  $-\text{Si}-\text{O}-\text{Si}((\text{CH}_3)_2)-$ ),  $0.36$ – $0.67$  (quint, 4.00 H (ref),  $-\text{Si}-\text{CH}_2-$ ),  $1.41$ – $1.84$  (m, 4.55 H,  $-\text{Si}-\text{CH}_2-\text{CH}_2-$ ),  $1.89$ – $2.16$  (m, 1.62 H,  $-\text{OH}$ ),  $3.21$ – $3.64$  (2 t, 8.09 H,  $-\text{Si}-\text{CH}_2-\text{CH}_2-\text{CH}_2-\text{O}-\text{CH}_2-\text{CH}_2-$ ),  $3.64$ – $3.96$  (m, 3.98 H,  $-\text{Si}-\text{CH}_2-\text{CH}_2-\text{CH}_2-\text{O}-\text{CH}_2-\text{CH}_2-\text{OH}$ )) and by gel permeation chromatography (GPC), as shown by the black graph in Figure 2h. Inspired by the protocol provided by S.K. Bhatia et al.,<sup>[40]</sup> 10 g (5.29 mmol, 1 eq.) of OH-PDMS was stirred overnight in a two-neck, round-bottom flask at 330 rpm, 81 °C and  $10^{-2}$  mbar to remove any residual water. The atmosphere was exchanged three times with Ar and 50 ml of dry hexane was added. The mixture was cooled in an Ar atmosphere to  $-20$  °C while stirring at 180 rpm. In total, 1.5 ml (11.0 mmol, 2.075 eq.) of triethylamine was added in one shot. After 15 minutes, 1.8 ml (10.8 mmol, 2.05 eq.) of triuromethanesulfonic anhydride was added and the activation of the terminal hydroxy-groups was left to proceed for 4 hours before adding excess potassium thioacetate in dry dimethylformamid (22.0 mmol, 4.1 eq.). The reaction mixture was left to stir overnight, followed by three extractions with water to yield a quantitative amount of a light-brown viscous liquid after evaporating the hexane, hereon referred to as "protected SH-PDMS." The NMR spectra of this protected SH-PDMS can be seen as the green-coloured graph in Figure 2 g: <sup>1</sup>H NMR (400 MHz,  $\text{CDCl}_3 + \text{K}_2\text{CO}_3$ ,  $\delta$ , ppm):  $-0.50$ – $0.35$  (m, 121.20 H,  $-\text{Si}-\text{O}-\text{Si}((\text{CH}_3)_2)-$ ),  $0.36$ – $0.67$  (quint, 4.00 H (ref),  $-\text{Si}-\text{CH}_2-$ ),



1.31–1.46 (t, 0.47 H, –SH), 1.41–1.84 (m, 4.24 H, –Si–CH<sub>2</sub>–CH<sub>2</sub>–), 1.89–2.16 (m, 0.28 H, –OH), 2.16–2.46 (s, 4.32 H, –S–C(O)–CH<sub>3</sub>), 2.82–3.25 (t, 3.07 H, –Si–CH<sub>2</sub>–CH<sub>2</sub>–CH<sub>2</sub>–O–CH<sub>2</sub>–CH<sub>2</sub>–S–C(O)–CH<sub>3</sub>), 3.21–3.64 (2 t, 8.19 H, –Si–CH–CH<sub>2</sub>–CH<sub>2</sub>–O–CH<sub>2</sub>–CH<sub>2</sub>–), 3.64–3.96 (m, 1.01 H, –Si–CH<sub>2</sub>–CH<sub>2</sub>–CH<sub>2</sub>–O–CH<sub>2</sub>–CH<sub>2</sub>–OH), with the corresponding green-coloured GPC curve in Figure 2g. To produce the terminal thiol functionality, 0.042 g (1.11 mmol, 2.1 eq.) of LiAlH<sub>4</sub> was dissolved in a 25 ml one-neck, round-bottom flask in 2 ml cold (ice bath) dry hexane and stirred at 200 rpm. In total, 1 g (0.53 mmol, 1 eq.) of thioacetate-modified PDMS was dissolved in cold (ice bath) dry hexane and added drop-wise to the stirred LiAlH<sub>4</sub>, followed by the addition of 4 ml of dry tetrahydrofuran to increase the solubility of the reaction partners, while deacetylation was left stirring for 3 hours in the ice bath before quenching the excess LiAlH<sub>4</sub> slowly with cold water. Triple extraction with water yielded 0.87 g of a golden, viscous liquid (unprotected SH-PDMS) after evaporating the hexane. The NMR spectra are shown as the blue-coloured curve in Figure 2f: <sup>1</sup>H NMR (400 MHz, CDCl<sub>3</sub> + K<sub>2</sub>CO<sub>3</sub>, δ, ppm): –0.50–0.35 (m, 148.37 H, –Si–O–Si((CH<sub>3</sub>)<sub>2</sub>–), 0.36–0.67 (quint, 4.00 H (ref), –Si–CH<sub>2</sub>–), 1.41–1.84 (m, 5.43 H, –Si–CH<sub>2</sub>–CH<sub>2</sub>–), 1.89–2.16 (m, 0.44 H, –OH), 2.59–2.79 (dt, 2.60 H, –CH<sub>2</sub>–S–S–CH<sub>2</sub>–), 3.21–3.64 (2 t, 7.82 H, –Si–CH<sub>2</sub>–CH<sub>2</sub>–CH<sub>2</sub>–O–CH<sub>2</sub>–CH<sub>2</sub>–), 3.64–3.96 (m, 0.6 H, –Si–CH<sub>2</sub>–CH<sub>2</sub>–CH<sub>2</sub>–O–CH<sub>2</sub>–CH<sub>2</sub>–OH), with the corresponding blue-coloured GPC graph in Figure 2h.

To assess the thermal stability of synthesized SH-PDMS, 100 mg was heated to 150 °C, far below the thermal decomposition temperature of the PDMS backbone<sup>[41]</sup> or methyl side group bonds,<sup>[42]</sup> and kept at this temperature for 40 minutes. The analysis of thermally treated SH-PDMS can be seen in the red-coloured <sup>1</sup>H NMR graph in Figure 2g: (400 MHz, CDCl<sub>3</sub> + K<sub>2</sub>CO<sub>3</sub>, δ, ppm): –0.50–0.35 (m, 153.64 H, –Si–O–Si((CH<sub>3</sub>)<sub>2</sub>–), 0.36–0.67 (quint, 4.00 H (ref), –Si–CH<sub>2</sub>–), 1.41–1.84 (m, 6.43 H, –Si–CH<sub>2</sub>–CH<sub>2</sub>–), 1.89–2.16 (m, 0.45 H, –OH), 2.59–2.79 (dt, 2.62 H, –CH<sub>2</sub>–S–S–CH<sub>2</sub>–), 3.21–3.64 (2 t, 7.99 H, –Si–CH<sub>2</sub>–CH<sub>2</sub>–CH<sub>2</sub>–O–CH<sub>2</sub>–CH<sub>2</sub>–S–), 3.64–3.96 (m, 0.94 H, –Si–CH<sub>2</sub>–CH<sub>2</sub>–CH<sub>2</sub>–O–CH<sub>2</sub>–CH<sub>2</sub>–OH) with the corresponding red-coloured GPC graph in Figure 2h.

The NMR and GPC spectra of supplied OH-PDMS indicate a chemically pure and homogeneously dispersed substance with an NMR-based number average molecular weight  $M_n$  of 1,733 g mol<sup>–1</sup> (the quintet at 0.36 to 0.76 served as a reference for 4 H in all spectra). After exchanging terminal hydroxy groups on OH-PDMS for thioacetate functionalities, a broad singlet within the NMR data at 2.16 to 2.41 ppm confirmed the modification. The corresponding integral of 4.42 suggests that the reaction yielded about 75% thioacetate functionality. The subsequent reduction with LiAlH<sub>4</sub> released acetate, which was removed in the water extraction phase and caused the disappearance of the respective singlet at 2.16 to 2.41 ppm (Figure 2g, blue-coloured spectra). Integrals corresponding to the signals from the dimethylsiloxane units at –0.50 to 0.35 ppm rose from 125 to 151 after deacetylation, confirming the shift of molecular weight distribution to increased molecular weights (corresponding GPC curves from green to blue colour in Figure 2h) and indicating disulphide bond formation after de-protection. The integrals of the spacer CH<sub>2</sub> groups are preserved for the reaction steps and characteristic shifts of the CH<sub>2</sub>-group, subsequently connected to –OH, –thioacetate and –SH have been observed. The signal of the unprotected terminal thiol groups seemed superposed with the signal of the CH<sub>2</sub> group and was therefore not clearly resolved but indirectly confirmed by the increase in the respective integral at 1.41 from 5.49 to 6.33 ppm, namely the blue- and red-coloured NMR spectra in Figure 2g, respectively. GPC analysis confirms the integrity of the polymer chains during the reaction steps, i.e. the thermal stability of the SH-PDMS at a temperature of 150 °C and a heating period of 40 minutes. A slight shift to increased molecular weights indicates chain elongation, due to disulphide bond formation (red-coloured graph in Figure 2h). SH-PDMS was thermally evaporated at a temperature of (140 ± 5) °C to avoid thermal degradation of the thiol groups above 150 °C.<sup>[20]</sup>

**Molecular beam deposition:** PDMS, Au, and Cr were thermally evaporated and deposited under ultra-high vacuum (UHV) conditions at

a base pressure of 10<sup>–7</sup> mbar. DMS-V05 and synthesized SH-PDMS were evaporated using low-temperature effusion cells (NTEZ, Dr. Eberl MBE Komponenten GmbH, Weil der Stadt, Germany) with a 25 cm<sup>3</sup> crucible for DMS-V05 and a 2 cm<sup>3</sup> crucible for SH-PDMS. High-temperature effusion cells (HTEZ, Dr. Eberl MBE Komponenten GmbH, Weil der Stadt, Germany) with 10 cm<sup>3</sup> PBN-crucibles were utilized for Au and Cr, while DMS-V05 thin films were evaporated at a crucible temperature of (200 ± 5) °C, well below the temperature of vinyl end groups thermal degradation.<sup>[9]</sup> Au and Cr were evaporated at temperatures ranging from 1400 to 1440 °C, corresponding to deposition rates of about 0.3 and 1.1 10<sup>–2</sup> nm s<sup>–1</sup>, respectively. Within the range of chosen deposition rates no distinct influence on Au nanoparticle formation was expected.<sup>[26]</sup> The Si substrate was mounted at a distance of 400 mm away from the crucibles and rotated at a speed of 5 rpm to obtain improved homogeneity.

**Ultraviolet cross-linking:** C-linking was initiated by in situ ultraviolet (UV) light irradiation from an externally mounted source (H2D2 light source L11798, Hamamatsu, Japan) through a CaF<sub>2</sub>-window.<sup>[8]</sup>

**Real-time spectroscopic ellipsometry:** To examine in situ the optical properties of the forming nanostructures, a spectroscopic ellipsometer (SE801, Sentech, Berlin, Germany) with SpectraRay3 software was utilized. Spectroscopic  $\psi$ - and  $\Delta$ -values in the range 190 to 1050 nm were monitored at a frequency between 0.5 to 2 Hz at an incident angle of 70° to the normal of the substrate's surface. The 4 mm diameter of incident beam resulted in a 4 × 10 mm<sup>2</sup> spot area on the substrate. Local heating, owing to plasmon-resonant absorption, can be neglected, as our setup with a diffuse halogen/deuterium lamp delivered radiation intensity by five orders of magnitude lower than compared to the radiation intensity of 19 W cm<sup>–2</sup> used for laser-based selective photo-thermal cancer therapy.<sup>[43]</sup> The obtained  $\psi$ - and  $\Delta$ -values, or the Fourier coefficients  $S_1$  and  $S_2$ , are related to the complex Fresnel reflection coefficients  $r_p$  and  $r_s$  of p- and s-polarized light and their ratio  $\rho$  by

$$\rho = r_p/r_s = \tan\Psi \cdot e^{i\Delta} \quad (1)$$

Based on the obtained Fresnel reflection coefficient ratio it is possible to extract the wavelength-dependent dielectric function  $\varepsilon(\lambda)$

$$\langle \varepsilon \rangle = \langle \varepsilon' \rangle + i \langle \varepsilon'' \rangle = \langle \tilde{n} \rangle^2 = (\langle n \rangle + i \langle k \rangle)^2 \\ = \varepsilon_0 \sin^2(\phi_0) \left[ 1 + \tan^2(\phi_0) \left( \frac{1-\rho}{1+\rho} \right)^2 \right] \quad (2)$$

with the angle of incidence  $\phi_0$ , the vacuum permittivity  $\varepsilon_0 = 1$  and  $n(\lambda)$  the real and  $k(\lambda)$  the imaginary parts of the refractive index, respectively.

To observe the growth and cross-linking of the evaporated PDMS, its dielectric function was modelled with the Tauc–Lorentz (TL) dispersion formula.<sup>[44]</sup> A Bruggeman effective medium model<sup>[44]</sup> (EMA) was included to obtain the surface roughness induced by the nucleation centres or polymer/metal interface layers. This layer is considered to have an effective dielectric or optical property deduced from equal fractional parts of deposited PDMS with refractive index  $n_i$  and void material  $n_e$ , cf. equation (3):

$$0 = \sum_{i=1}^N f_i \frac{n_i^2 - n_e^2}{n_i^2 + 2n_e^2} \quad (3)$$

The EMA is applicable if the grown film fulfils two key assumptions: First, the surface roughness/nucleation centres are smaller than the minimum wavelength, in order to ignore light scattering, and second, the dielectric function is size- and shape-independent. The thermally evaporated PDMS fulfils these assumptions. For data evaluation the void fraction was set to 0.5.<sup>[44]</sup>

To model the dielectric function of the utilized noble metals a Drude–Lorentz (DL) oscillator model was applied. Although the enhanced flexibility of Gaussian oscillators is mentioned in the literature,<sup>[45]</sup>



we found DL oscillators modelled precisely the optical properties of nucleating Au nanoparticles. This is a combination of two dispersion types: first, the Drude absorption of free charge carriers, assuming that they act in phase in response to the applied electric field, and second, the Lorentz oscillator, effectively describing the electrons bound to a positive ion core.<sup>[29]</sup>

For the assessment of the model the mean square error (MSE) of the divergence from the obtained fit to the acquired data was calculated. The MSE is defined according to the figure of merit as

$$\text{MSE} = \frac{1}{N} \sqrt{\sum_{i=1}^N \left[ \left( \frac{\Psi_i^{\text{mod}} - \Psi_i^{\text{exp}}}{\sigma_{\Psi_i}^{\text{exp}}} \right)^2 + \left( \frac{\Delta_i^{\text{mod}} - \Delta_i^{\text{exp}}}{\sigma_{\Delta_i}^{\text{exp}}} \right)^2 \right]} \quad (4)$$

with the random and systematic error  $\sigma$ .

**Atomic force microscopy:** The surface topography of the thermally evaporated nanostructures was scanned using atomic force microscopy (AFM). The AFM system (FlexAFM C3000, Nanosurf AG, Switzerland) was operated in tapping mode using a soft cantilever (Tap190Al-G probe, NanoAndMore GmbH, Wetzlar, Germany). Areas of  $5 \times 5 \mu\text{m}^2$  were scanned with a vibration amplitude of 2 V and a set point of 20%. In total, 512 lines at a speed of 1 s per line were acquired for each image. The root-mean-squares values were calculated using Gwyddion 2.41 software (Gwyddion: Open-source software for SPM data analysis, <http://gwyddion.net>).

**Nanoparticle segmentation:** To segment the Au clusters, the AFM images were flattened by adaptive local histogram equalization implemented in MATLAB (The MathWorks, Inc., Natick, USA). Subsequently, pixels belonging to the clusters were separated from the background via thresholding.

**Nuclear magnetic resonance analysis:**  $^1\text{H-NMR}$  spectra were recorded on a Bruker DPX-400 spectrometer in deuterated chloroform without tetramethylsilane. The analysis (phase correction and Wittaker Smoother to adjust the baseline) was performed in MestReNova 10.0.1-14719 (Mestrelab Research S.L., Spain).

**Gel permeation chromatography:** Gel permeation chromatography traces were recorded using WinGPC (v8.20 build 4815) connected to an Agilent 1200 system equipped with a refractive index detector (RI) and a series of analytical SDV columns (pre-column (5 cm),  $1\text{e}^3 \text{ \AA}$  (30 cm) and  $1\text{e}^5 \text{ \AA}$  (30 cm), all  $5 \mu\text{m}$  particles and 0.8 cm in diameter, PSS, Germany). The columns and RI were kept at  $35 \text{ }^\circ\text{C}$ , and the system was operated using THF as eluent at a flow rate of  $1 \text{ ml s}^{-1}$  and calibrated against narrow distributed polystyrene standards.

## Supporting Information

Supporting Information is available from the Wiley Online Library or from the author.

## Acknowledgements

The financial contributions of the Schweizerischer Nationalfonds zur Förderung der Wissenschaftlichen Forschung (project 200021-t135496), of the nano-tera.ch initiative (project SmartSpincter), and of the Swiss Nanoscience Institute (SNI) for the AFM, is gratefully acknowledged.

T.T. conceived the idea and initiated the ellipsometric experiments. B.M. guided the research and structure of the study. S.L. synthesised the tailored SH-PDMS and conducted gel permeation chromatography and the nuclear resonance analysis. B.O. and H.D. conducted the atomic force microscopy experiments and analysis, respectively. H.D., T.P. and V.L. assisted T.T. and B.M. with the analysis and related discussion. T.T., V.L. and B.M. wrote the manuscript.

## Conflict of Interest

The authors declare no conflict of interest.

## Keywords

nanometer-thin gold films, organic molecular beam deposition, polydimethylsiloxane self-assembly, spectroscopic ellipsometry

Received: February 16, 2017

Revised: March 29, 2017

Published online: June 12, 2017

- [1] J. A. Rogers, T. Someya, Y. Huang, *Science* **2010**, *327*, 1603.
- [2] H. F. Mark, *Encyclopedia of Polymer Science and Technology*, Vol. 15, Wiley & Sons, Hoboken, NJ **2014**.
- [3] A. Hirsch, H. O. Michaud, A. P. Gerratt, S. de Mulatier, S. P. Lacour, *Adv. Mater.* **2016**, *28*, 4507.
- [4] J. C. McDonald, G. M. Whitesides, *Acc. Chem. Res.* **2002**, *35*, 491.
- [5] B. Zhang, Q. Dong, C. E. Korman, Z. Li, M. E. Zaghoul, *Sci. Rep.* **2013**, *3*, 1098.
- [6] F. B. Madsen, A. E. Daugaard, S. Hvilsted, A. L. Skov, *Macromol. Rapid Commun.* **2016**, *37*, 378.
- [7] P. Brochu, Q. Pei, *Macromol. Rapid Commun.* **2010**, *31*, 10.
- [8] T. Töpfer, F. Weiss, B. Osmani, C. Bippes, V. Leung, B. Müller, *Sensor Actuat. A Phys* **2015**, *233*, 32.
- [9] T. Töpfer, S. Lörcher, F. Weiss, B. Müller, *APL Mater.* **2016**, *4*, 056101.
- [10] F. M. Weiss, T. Töpfer, B. Osmani, S. Peters, G. Kovacs, B. Müller, *Adv. Electron. Mater.* **2016**, *2*, 1500476.
- [11] E. Ozbay, *Science* **2006**, *311*, 189.
- [12] P. Guo, R. D. Schaller, J. B. Ketterson, R. P. H. Chang, *Nat Photon.* **2016**, *10*, 267.
- [13] F. Bisio, R. Proietti Zaccaria, R. Moroni, G. Maidecchi, A. Alabastri, G. Gonella, A. Giglia, L. Andolfi, S. Nannarone, L. Mattered, M. Canepa, *ACS Nano* **2014**, *8*, 9239.
- [14] R. T. Hill, *Wiley Interdiscip. Rev.: Nanomed. Nanobiotechnol.* **2015**, *7*, 152.
- [15] M. K. Chaudhury, J. Ashes, *Sci. Technol.* **1993**, *7*, 669.
- [16] a) A. Manjavacas, F. J. Garcia de Abajo, *Nat Commun.* **2014**, *5*, 1; b) N. Stokes, A. M. McDonagh, M. B. Cortie, *Gold Bull.* **2007**, *40*, 310.
- [17] M. Grzelczak, J. Perez-Juste, P. Mulvaney, L. M. Liz-Marzan, *Chem. Soc. Rev.* **2008**, *37*, 1783.
- [18] S. K. Ghosh, T. Pal, *Chem. Rev.* **2007**, *107*, 4797.
- [19] H. L. Zhang, S. D. Evans, J. R. Henderson, *Adv. Mater.* **2003**, *15*, 531.
- [20] A. Chandekar, S. K. Sengupta, J. E. Whitten, *Appl. Surf. Sci.* **2010**, *256*, 2742.
- [21] H. Grönbeck, A. Curioni, W. Andreoni, *J. Am. Chem. Soc.* **2000**, *122*, 3839.
- [22] S. Al-Maawali, J. E. Bemis, B. B. Akhremitchev, R. Leecharoen, B. G. Janesko, G. C. Walker, *J. Phys. Chem. B* **2001**, *105*, 3965.
- [23] N. B. Cramer, S. K. Reddy, M. Cole, C. Hoyle, C. N. Bowman, *J. Polym. Sci. Pol. Chem.* **2004**, *42*, 5817.
- [24] B. Osmani, T. Töpfer, C. Deschenaux, J. Nohava, F. M. Weiss, V. Leung, B. Müller, in *AIP Conf. Proc.*, Vol. 1646, AIP Publishing, Thessaloniki, **2015**, 91.
- [25] N. Bowden, S. Brittain, A. G. Evans, J. W. Hutchinson, G. M. Whitesides, *Nature* **1998**, *393*, 146.
- [26] R. Gupta, M. J. Dyer, W. A. Weimer, *J. Appl. Phys.* **2002**, *92*, 5264.
- [27] X. D. Li, T. P. Chen, Y. Liu, K. C. Leong, *Opt. Express* **2014**, *22*, 5124.
- [28] P. Romaniello, P. L. de Boeij, *J. Chem. Phys.* **2005**, *122*, 164303.

- [29] T. W. H. Oates, H. Wormeester, H. Arwin, *Prog. Surf. Sci.* **2011**, *86*, 328.
- [30] M. Hövel, B. Gompf, M. Dressel, *Phys. Rev. B* **2010**, *81*, 035402.
- [31] S. Eustis, M. A. El-Sayed, *Chem. Soc. Rev.* **2006**, *35*, 209.
- [32] N. G. Khlebtsov, L. A. Dykman, *J. Quant. Spectrosc. Radiat. Transfer* **2010**, *111*, 1.
- [33] T. W. H. Oates, L. Ryves, M. M. M. Bilek, *Opt. Express* **2008**, *16*, 2302.
- [34] Y. Xue, X. Li, H. Li, W. Zhang, *Nat Commun.* **2014**, *5*, 4348.
- [35] B. Osmani, H. Deyhle, F. M. Weiss, T. Töpfer, M. Karapetkova, V. Leung, B. Müller, *Proc. SPIE* **2016**, *9798*, 979822.
- [36] S. Olcum, A. Kocabas, G. Ertas, A. Atalar, A. Aydinli, *Opt. Express* **2009**, *17*, 8542.
- [37] T. V. Teperik, F. J. Garcia de Abajo, A. G. Borisov, M. Abdelsalam, P. N. Bartlett, Y. Sugawara, J. J. Baumberg, *Nat. Photon.* **2008**, *2*, 299.
- [38] E. Fattorini, T. Brusa, C. Gingert, S. E. Hieber, V. Leung, B. Osmani, M. D. Dominietto, P. Büchler, F. Hetzer, B. Müller, *Ann. Biom. Eng.* **2016**, *44*, 1355.
- [39] a) D. Rus, M. T. Tolley, *Nature* **2015**, *521*, 467; b) I. A. Anderson, T. A. Gisby, T. G. McKay, B. M. O'Brien, E. P. Calius, *J. Appl. Phys.* **2012**, *112*, 041101.
- [40] S. K. Bhatia, J. Hajdu, *Tetrahed. Lett.* **1988**, *29*, 31.
- [41] K. Chenoweth, S. Cheung, A. C. T. van Duin, W. A. Goddard, E. M. Kober, *J. Am. Chem. Soc.* **2005**, *127*, 7192.
- [42] G. Deshpande, M. E. Rezac, *Polym. Degrad. Stab.* **2002**, *76*, 17.
- [43] I. H. El-Sayed, X. Huang, M. A. El-Sayed, *Cancer Lett.* **2006**, *239*, 129.
- [44] H. Fujiwara, *Spectroscopic Ellipsometry: Principles and Applications*, John Wiley & Sons, Hoboken, NJ **2007**.
- [45] M. Loncaric, J. Sancho-Parramon, H. Zorc, *Thin Solid Films* **2011**, *519*, 2946.
- [46] L. De Sio, R. Caputo, U. Cataldi, C. Umeton, *J. Mater. Chem.* **2011**, *21*, 18967.
- [47] J. N. Anker, W. P. Hall, O. Lyandres, N. C. Shah, J. Zhao, R. P. Van Duyne, *Nat. Mater.* **2008**, *7*, 442.
- [48] P. B. Johnson, R. W. Christy, *Phys. Rev. B* **1974**, *9*, 5056.
- [49] A. Baba, K. Imazu, A. Yoshida, D. Tanaka, K. Tamada, *SpringerPlus* **2014**, *3*, 1.
- [50] E. D. Palik, *Handbook of Optical Constants of Solids III*, Academic, New York **1998**.